Vol. 25(1994) *ACTA PHYSICA POLONICA B* No 3–4

RECENT RESULTS FROM THE PROJECTILE FRAGMENT SEPARATOR FRS*

G. Münzenberg

Gesellschaft für Schwerionenforschung mbH
Planckstr. 1, D 64220 Darmstadt, Germany

(Received August 28, 1993)

Systematic studies of peripheral nuclear collisions such as the fragmentation of relativistic projectiles up to uranium and uranium fission are reported as well as the preparation of isotopic beams of exotic nuclei, ranging from light neutron-rich drip line nuclei to the fission of exotic nuclei near uranium, for secondary-beam experiments with the fragment separator FRS. Experiments in the experimental storage ring ESR with cooled secondary-beams will be discussed. We will give an outline of the prospects of secondary-beam physics at relativistic energies.

PACS numbers: 25.75. +r, 25.60. +v

1. Introduction

The fragmentation of relativistic heavy ions in peripheral nuclear collisions is not only a method to create exotic nuclei at energies far above the Coulomb barrier, suitable for secondary nuclear reactions, but also a nuclear reaction interesting in itself. At the GSI projectile fragment separator FRS projectile fragments as heavy as uranium for the first time were separated in-flight. The fragmentation of heavy nuclei was studied throughout the whole periodic table from oxygen to uranium and with energies starting from 500 MeV/u. Reaction cross-sections and kinematics were investigated systematically. The results are compared to improved spallation systematics and to macroscopic as well as microscopic models such as the abrasion-ablation model and intranuclear cascade calculations. Coulomb fission at relativistic energies seems a promising process for the production of neutron-rich isotopes and will give new insights in the fission process. Due to their strong

---

* Presented at the XXIII Mazurian Lakes Summer School on Nuclear Physics, Piaski, Poland, August 18–28, 1993.

kinematic focusing relativistic fission fragments are effectively collected with FRS.

The use of secondary-beams with energies above Coulomb barrier will give new insights in nuclear structure and help to complete our knowledge of exotic nuclei which is predominantly based on nuclear decay studies. We measured nuclear breakup reactions and elastic proton scattering in reversed kinematics for light nuclei near the neutron drip line to investigate the neutron halo and to extract nuclear matter density distributions for weakly bound systems. Fragmentation of secondary-beams to measure the evaluation of the charge changing cross-sections in dependence of the proton abundance in the projectile is related to the proton separation energy. Experiments on the induced fission of exotic uranium fragments will have new impacts on the understanding of nuclear structure, *e.g.* near the 126 neutron shell.

Detailed studies of nuclear structure and nuclear reactions involving secondary-beams will be possible with the experimental setups in the target hall with the 4π and the K caves (Fig. 1), which are equipped with the ALADIN magnet, the LAND large area neutron detector, the KAOS spectrometer and, in future, with the Heidelberg crystal ball. Secondary-beam physics inside the storage and cooler ring ESR will start a new generation of experiments. First tests for direct mass measurements of short-lived exotic nuclei and β-decay studies of bare, hydrogen- or helium like nuclei coasting in the ESR have been carried out. Electron cooling will provide beams of high density in phase space, which makes it possible to carry out high precision experiments. Typical experiments are direct reactions in reversed kinematics with the internal gas target of the ESR.

2. Preparation of relativistic isotopic beams of exotic nuclei with FRS

The FRS is a versatile forward magnetic spectrometer. It can be operated in a high resolution mode or as an in-flight separator for isotopically clean secondary-beams (Fig. 1). The maximum bending power of 18 Tm is adapted to the full SIS energy. The separator consists of four ion-optically identical sections. Resolution, solid angle and transmitted momentum spread are varied by appropriate settings of the quadrupole units to operate the separator, *e.g.* in the nondispersive high transmission mode as an achromatic system or as a highly resolving spectrometer to be used with the cooled beams re-injected from ESR into SIS. Besides the exit to the dedicated FRS detector area, the FRS has an exit to inject secondary-beams into the storage ring and a direct exit to the target hall beamline.

The principal application of the separator is the preparation of isotopic beams of exotic nuclei produced by projectile fragmentation. The combina-

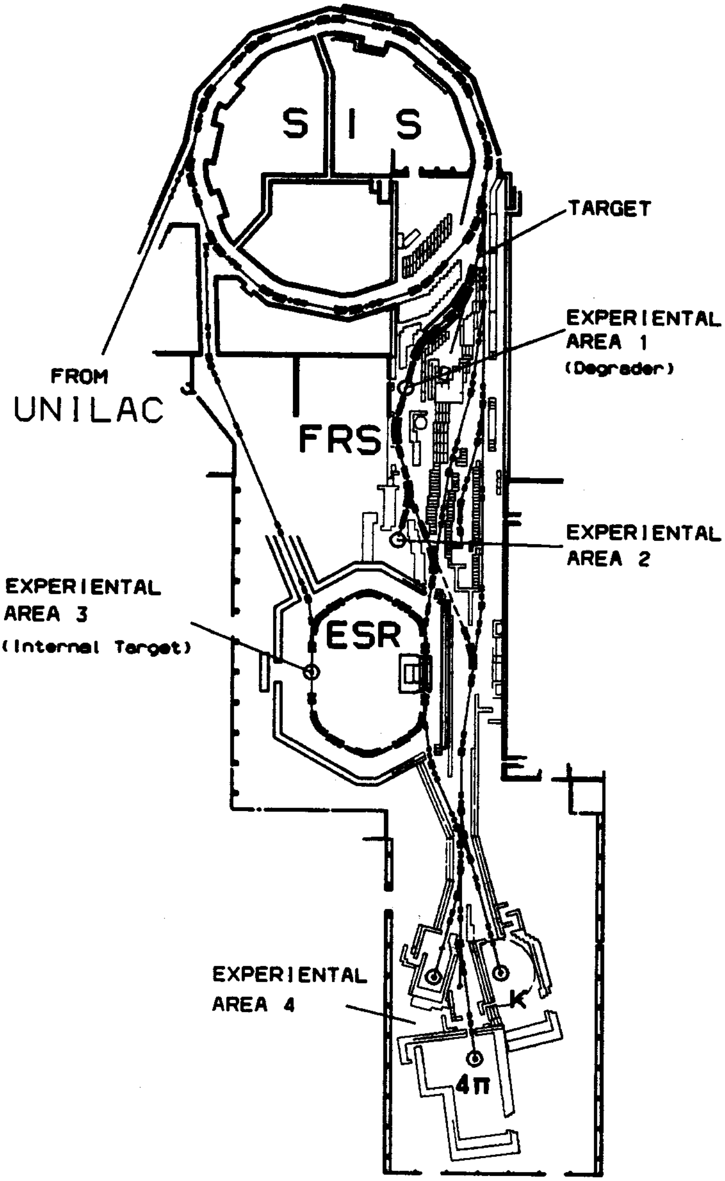

Fig. 1. The layout of the GSI facility for the investigation of relativistic heavy ions. The target areas for secondary-beam experiments are indicated.

tion of reaction kinematics and magnetic deflection allows to separate along cuts of constant A/Z ratio in the nuclear table.

$$B\rho = \beta\gamma \, \frac{A}{Z} \approx \frac{A}{Z} \quad \text{for} \quad \beta\gamma = \text{const}\,. \tag{1}$$

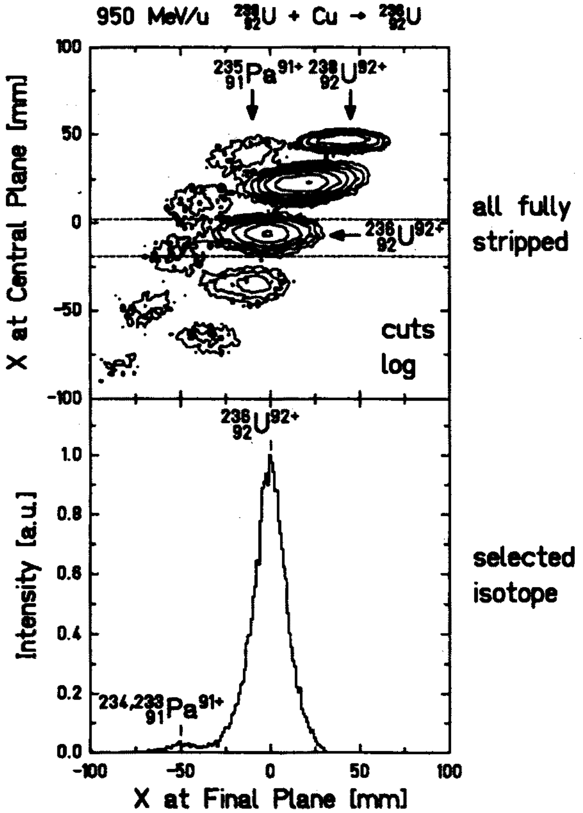

Fig. 2. First isotopic separation of relativistic uranium fragments. Upper panel: The position distribution of the uranium fragments at the dispersive midplane is plotted versus the position at the exit, lower panel: Isotopically separated ^{236}U [3].

In this mode, large scale investigations such as measurements of isotopic production cross-sections and reaction kinematics, or gross properties like nuclear masses and deformations allow to study whole regions of the nuclear table. For the preparation of isotopic beams additional Z separation is achieved by introducing matter at the dispersive focal plane of FRS [1, 2]. The separation of projectile fragments up to uranium with energies from 0.5 MeV·A to 1 GeV·A was investigated systematically. Fig. 2 shows the separation of uranium isotopes from fragmentation of ^{238}U at 950 MeV·A in a 205 mg/cm^2 copper target and with a 5.3 g/cm^2 aluminum degrader displayed in a two-dimensional plot of the coordinate at the dispersive focal plane versus the exit position. Isotopic beams can be prepared after insertion of appropriate diaphragms, as indicated in the figure. It is noteworthy to mention that contaminants from hydrogen-like uranium are still a problem even at this high energy [3]. We could also demonstrate the first isotopic separation of relativistic uranium-fission products. Their in-flight separation is difficult as their broad momentum distributions affect the separation quality. Fig. 3 shows a cut through the light and heavy groups with the nuclear charge distribution well resolved; an example of the mass resolution for the strontium isotopes is shown in Fig. 4 [4].

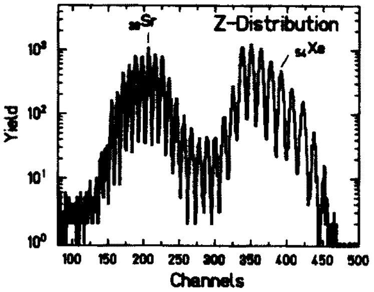

Fig. 3 Nuclear charge spectrum of uranium fission products created in a lead target [4].

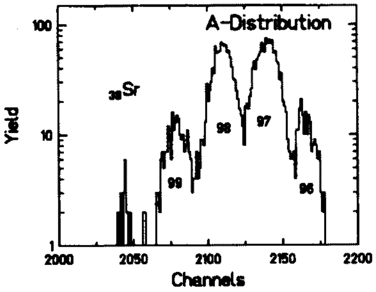

Fig. 4 Mass spectrum for strontium isotopes [4].

3. Projectile fragmentation — studies of peripheral collisions

3.1. *Cross-sections*

Projectile fragmentation is a two step process and can be described with the abrasion-ablation model. During the collision of two relativistic nuclei, in the overlapping zone of the interacting nuclei, highly excited nuclear matter is created, which separates the weakly excited parts of target and projectile outside the interaction region. They act as spectators and are excited to comparatively low temperatures of the order of 5 MeV. The excitation energy is dissipated predominantly by particle emission. In the energy regime of limiting fragmentation [5] above 100 MeV·A, reaction cross-sections depend on the geometric size of the interacting nuclei independent of energy.

We studied systematically fragmentation cross-sections and reaction kinematics, at energies between 500 MeV·A and 1000 MeV·A, for light, medium, and heavy projectiles as ^{18}O, ^{86}Kr [6], ^{129,136}Xe [7], ^{197}Au [8], and ^{238}U, including fission [4]. The results were analyzed in the frame

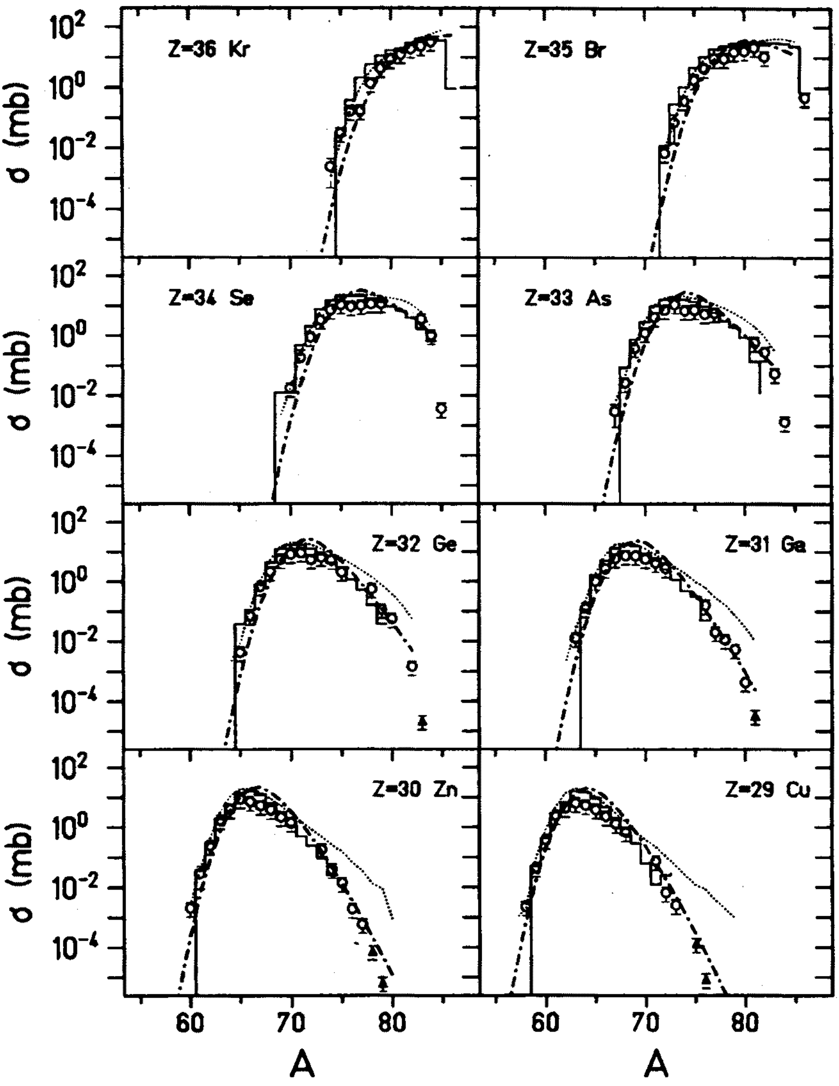

Fig. 5. Isotopic distributions for 500 MeV/u ^{86}Kr fragments [6]. The experimental data (symbols) are compared to the semiempirical prediction (dashed-dotted line) [11], the abrasion-ablation model (dotted line) [15] and the intranuclear cascade calculations (histogram) [17].

of semiempirical descriptions, abrasion-ablation, and intranuclear cascade-evaporation models, respectively. Projectile fragmentation, being the kinematically inverse process of the proton-induced spallation, can be described on the basis of the semiempirical description of Rudstam [9] or the more general approach of Silberberg and Tsao [10]. Here we use the improved semiempirical model EPAX [11]. A comparison between the experimental isotopic production cross-sections for the elements between krypton and copper, produced by fragmentation of 500 MeV/u ^{86}Kr [6], and EPAX shows good agreement except for the most neutron-rich isotopes where the cross-sections are overestimated (dashed-dotted line in Fig. 5). It is noteworthy to mention that the neutron-rich ^{86}Kr, four mass units from the β stability line, shifts the maximum of the fragment distributions in the vicinity of the projectile to neutron-rich isotopes. The inclusion of this "memory effect" into the systematics by Sümmerer gives the perfect reproduction for the krypton fragments. The memory effect was also verified in a comparative study of ^{129}Xe and ^{136}Xe [12] fragmentation.

Theoretical models use the macroscopic [13] or the microscopic description [14]. Recently, an improved approach in the frame of the abrasion-ablation model has been developed [15]. The abrasion part yields the number of abraded nucleons from the geometrical overlap between target and projectile, determined by the impact parameter. The neutron-to-proton ratio is obtained using the hypergeometrical distribution which anticipates no correlation between abraded neutrons and protons. The number of vacancies created in the Fermi distribution determines the excitation energy of the prefragments. In this model, it is 13.3 MeV per particle-hole on the average (dotted line in Fig. 5) [15]. The evaporation in the ablation step is treated in terms of an improved transport model [16], or, optionally, by an evaporation code. To reproduce the experimental data the twofold excitation energy of 26 MeV per abraded nucleon must be used, as was shown for Au and Kr fragments [8]. This value, also necessary to reproduce our gold and xenon data, is in good agreement with BUU calculations [18]. The additional heating of the participant is caused by energetic nucleons from the fireball penetrating into the spectator [8] where they dissipate their energy.

The microscopic approach [17] treats single nucleon-nucleon interactions of the colliding systems with the intranuclear cascade code ISABEL [19]. The calculations include Pauli blocking, the Fermi gas distribution, and nucleonic excitation via the lowest lying Δ resonance. As we consider only peripheral collisions, mean field or compression effects, as in the more refined BUU and VUU models, are not taken into account. For the deexcitation of the prefragments the PACE code [20] which includes preequilibrium processes such as the emission of fast particle cascades can treat excitation energies in excess of 300 MeV. Again, the comparison to our experimental data (histogram in Fig. 5) shows excellent agreement. The INC calculation properly treats proton stripping, *e.g.* for ^{85}Br and ^{84}Se, and charge exchange reactions [21].

Systematic studies of the fragmentation cross-sections are important *e.g.* for astrophysics in context with the propagation of cosmic rays through interstellar matter or for biomedical applications.

3.2. Fission

Besides the fragmentation, Coulomb breakup at relativistic energies is an important process. It goes via the electromagnetic excitation of the giant dipole resonance located near 15 MeV for heavy nuclei. Coulomb induced, cold fission is extremely suited for the production of neutron-rich species. The data from a first systematic investigation of uranium fission following electromagnetic excitation and fragmentation, respectively, are under evaluation. We observe extremely neutron-rich isotopes of the light and heavy groups and could identify about 30 new isotopes in the gap between the light and the heavy fission group [4].

4. Reaction kinematics

The energy dissipation in the nuclear collision causes a downshift of the average fragment velocity with respect to the projectile. The statistically superimposed momentum distributions of the abraded or evaporated particles, respectively, are reflected in the momentum spread of the fragments. Fig. 6 shows the shift of the longitudinal momenta of ^{129}Xe fragments with 790 MeV·A [12]. The experimental slope parameter is 8 MeV/(c u) — a similar value was obtained for krypton [6] — in accordance with the collective tube model of Morrissey [22] predicting:

$$\langle \delta p_{\|} \rangle = 8(A_p - A_f)\ \mathrm{MeV}/c\,. \tag{2}$$

For the xenon isotopes a slope parameter of 16 MeV/(c u) was measured. The width of the final fragment momentum distribution is according to the semiempirical description of Morrissey [22]:

$$\sigma_{p_{\|}} = 87\sqrt{A_p - A_f}\ \mathrm{MeV}/c\,. \tag{3}$$

For cold fragmentation occurring in extremely peripheral collisions, such as proton removal, the momentum spread reflects the superposition of the Fermi momenta of the abraded nucleons. The independent particle model of Goldhaber [23] predicts:

$$\sigma_{p_{\|}} = p_F\sqrt{\frac{A_p - A_f}{5(A_p - 1)}}\,. \tag{4}$$

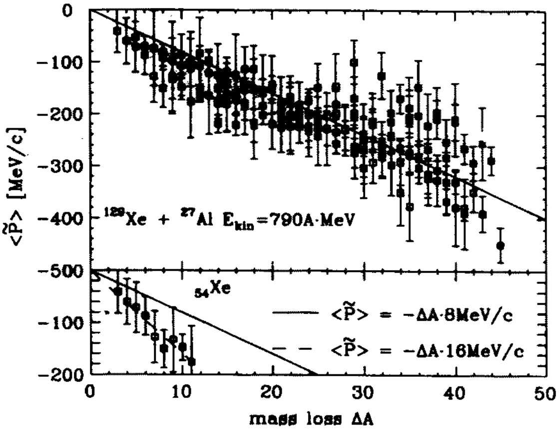

Fig. 6. Downshift of the parallel momentum of the fragments referred to the projectile. The prediction from Morrissey [22] (solid line), is compared to the experimental data from the fragmentation of ^{129}Xe at 790 MeV/u. Upper panel: all identified isotopes, lower panel: only xenon isotopes [12].

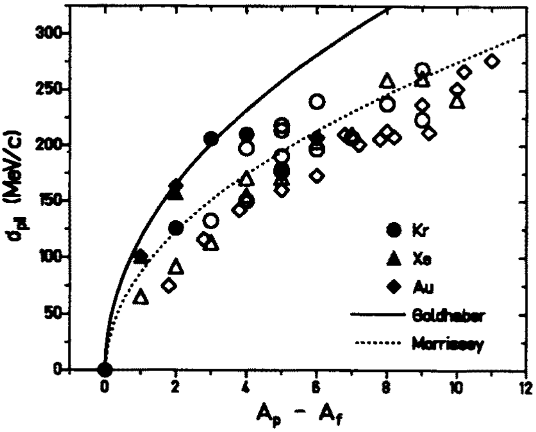

Fig. 7. Longitudinal momentum distributions for fragments from 500 MeV/u ^{86}Kr, 800 MeV/u ^{136}Xe and 1000 MeV/u ^{197}Au, respectively; full symbols: proton removal, open symbols: evaporation channels. The solid line follows the Goldhaber model, the dotted line — the semiempirical prediction of Morrissey.

Fig. 7 shows the momentum spreads for ^{86}Kr fragments with 500 MeV/u, ^{136}Xe fragments of 800 MeV/u, and ^{197}Au fragments of 1 GeV/u. The full symbols for proton removal follow the Goldhaber model displayed as solid line, with a Fermi momentum of $P_F = 260$ MeV/c from electron scattering data. The open symbols follow the sytematics of Morrissey indicated by a dotted line. The predicted momentum spread is too high by about 10%.

5. Secondary-beams

5.1. Skins and halos

In his pioneering experiments with relativistic secondary-beams of exotic light nuclei, Tanihata [24] discovered unusually large interaction cross-sections of weakly bound nuclei near the neutron drip line, such as ^{11}Li. This result could be explained in terms of the "neutron halo". The density distributions from a Hartree-Fock calculation [25] in ^{11}Li are displayed in Fig. 8 for the ^{9}Li core and the halo neutrons, respectively. The two weakly bound neutrons form a long tail of a low density neutron gas extending far outside the ^{9}Li core [26]. The insert displays a comparison between the total cross-section and the charge-changing cross-section for the neutron-rich lithium isotopes [27] interacting with a carbon target at 80 MeV/u. The strong increase of the total cross-section towards ^{11}Li is caused by the neutron halo, the charge changing cross-section does not vary.

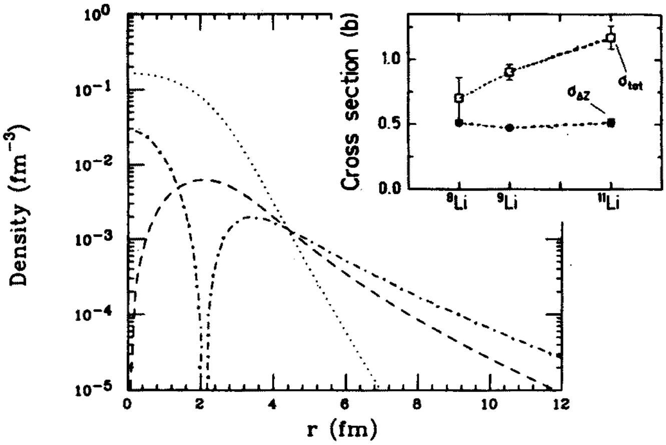

Fig. 8. Density distributions in ^{11}Li for the core (dotted line) and the halo neutrons calculated for $2s_{1/2}$ (dashed-dotted) and $1p_{1/2}$ (dashed) states, respectively. Insert: Comparison of total and charge-changing cross-sections for ^{8,9,11}Li (from Hansen [26]).

The question immediately arises whether halos or skins can be observed also for heavier systems or near the proton drip line. Tanihata found a correlation between skin thickness and the difference between the Fermi surfaces for neutrons and protons. The result of a relativistic mean field calculation is given in Fig. 9 [28]. For stable nuclei the Fermi surfaces are almost equal due to the about equal neutron and proton separation energies of about 8 MeV. Nuclei far off stability show large differences in the proton-

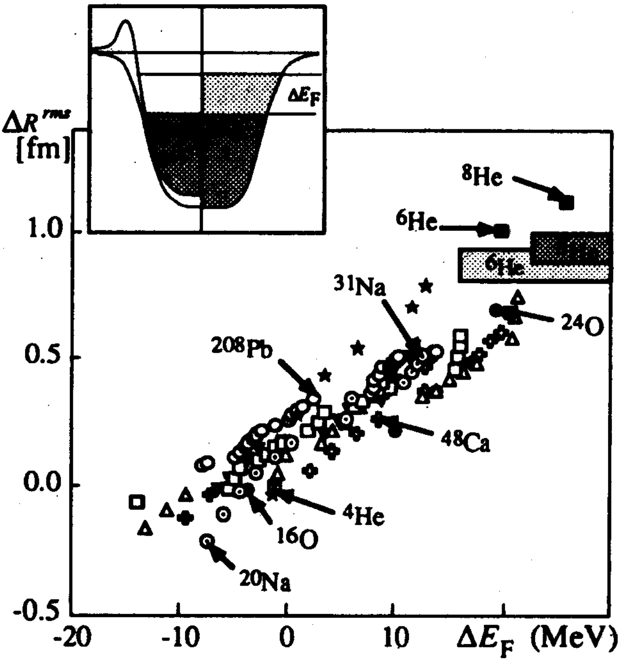

Fig. 9. Correlation between the difference of the Fermi levels between neutron and proton surfaces and the skin thickness, from a relativistic mean field calculation (from Tanihata [28]).

and neutron binding energies which is reflected by the differences between the corresponding Fermi surfaces. Neutron skins are expected for *e.g.* ^{31}Na at the N = 20 shell and for ^{24}O; proton skins for ^{20}Mg, located at the drip line, four protons above the doubly magic ^{16}O. There are proposals to measure the nuclear absorption radii of these nuclei at the FRS [29, 30].

5.2. Matter distributions

High-energy proton scattering is a well known tool to study nuclear matter distributions. One reason is that 500 MeV protons have a wavelength of 0.2 fm, much smaller than the spacing between the nucleons. The nucleon-nucleon cross-sections are energy independent. Above the Fermi energy there is no nuclear rearrangement during the passage through the nucleus. Collisions between two nucleons can be treated as two-body interactions and the data can be interpreted in terms of the Glauber model using the eikonal approach and free-nucleon cross-sections.

Matter distributions of instable nuclei are studied in reversed kinematics with relativistic secondary-beams directed on *e.g.* a proton target. Up to now, elastic proton scattering with exotic nuclei was investigated at comparatively low energies [31]. Recently, an experiment to study the matter density distributions for ^{4,6,8}He at 700 MeV/u has been carried out at the FRS by the Gatchina group, using the IKAR time projection chamber as an active target. The isotopically separated fragments are tracked eventwise by multiwire chambers to define their angles before and after the IKAR, respectively, where angle and energy of the elastically scattered protons are detected. We aim at an absolute accuracy of less than 5% of the differential cross-section for small momentum transfers of 1 MeV $\leq T_{\mathrm{recoil}} \leq$ 11 MeV [33].

5.3. Momentum distribution and binding energy

According to the Heisenberg uncertainty principle, the extension of the wave function and the width of the momentum distribution for a nucleon in a specific nuclear state are correlated. For an s-state neutron of the separation energy S_n the external wave function is a Yukawa function proportional to $\exp(-r/\rho)/r$ with the decay length $\rho = \hbar/\sqrt{2\mu S_n}$.

The momentum distributions of halo neutrons were investigated with various methods, either by measuring the longitudinal momentum distributions of the fragments after neutron removal using magnetic separators, or by extraction of transversal momenta from the angular distributions using neutron detectors, respectively. A kinematically complete experiment on the dissociation of ^{11}Be and ^{11}Li at energies of 280 MeV/u, 460 MeV/u and 680 MeV/u, respectively, has been carried out at GSI in two companion experiments. The longitudinal momentum distributions were measured at the fragment separator in the energy-loss mode with the secondary targets, aluminium and lead, placed at the dispersive central plane [34]. A compilation of our results and the experimental data from other laboratories are given in Table I.

TABLE I

Experimental momentum distributions from ^{11}Be and ^{11}Li breakup (f: fragment, n: neutron). The beam energies are given in brackets. See also Ref. [26].

	$\Delta p_{\parallel}$, (FWHM) [MeV/c]		$\Delta p_{\perp}$, (FWHM) [MeV/c]			
	FRS (f) (Al)	MSU [32] (f)	LAND (n) (C)	 (Pb)	GANIL [36] (n) (Be)	RIKEN [29] (f) (C)
^{11}Be	48 (680)		78 (460)	61 (460)	63 (41)	59 (800)
^{11}Li	43 (680)	50 (65)	28 (280)	23 (280)	24 (66)	47 (800)

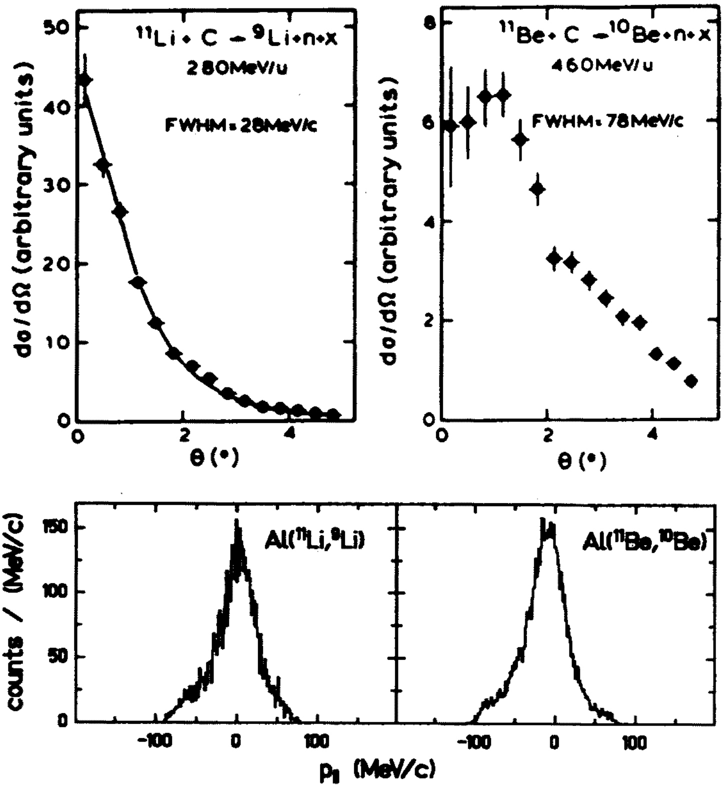

Fig. 10. Upper panels: Single neutron angular distributions after one and two neutron breakup of ^{11}Li and ^{11}Be, respectively, in a carbon target [35]. Lower panels: longitudinal momentum spreads for the daughter fragments of the same nuclei, measured with aluminum targets and operating FRS in the energy-loss mode [34].

The neutron angular distributions, neutron angular correlations, and the neutron-fragment correlations were measured with the combination of the ALADIN magnet and LAND large area position-sensitive neutron detector [35]. The fragment beams were separated by FRS and transported through the ESR. Fig. 10 shows the preliminary results from this experiment. The angular distribution for ^{11}Li can be well described by a Lorentzian. The halfwidth of the neutron angular distribution for 23 MeV, measured with the lead target, corresponds to a range parameter of $\rho = 13$ fm of a Yukawa wave function, in good agreement with earlier results for lower energies [31].

6. Nuclear structure - experiments with stored and cooled beams of exotic nuclei

6.1. Gross properties

Presently, there exists no fundamental nuclear model to describe nuclear properties such as ground state mass and deformation or half-life with sufficient precision. Therefore the measurement of gross nuclear properties such as drip lines, half-lives and decay modes, and the evaluation of the nuclear mass surface and ground state deformations at large scale is necessary to stringently test nuclear models which, for instance, have large impact on astrophysical models to describe the production and constitution of the chemical elements in the cosmos. As has been shown, for instance, in our experiments on the heaviest elements, such basic information can be already obtained from a small number of atoms, a clean identification provided. In-flight identification and correlation technique allow to measure with high sensitivity, on the basis of few atoms, gross properties of exotic nuclei: principal decay mode, branching ratios, half-live, and mass. As an example of a first experiment in the vicinity of ^{78}Ni, Fig. 11 displays the half-life measurement of the hitherto unknown isotope ^{65}Fe [38].

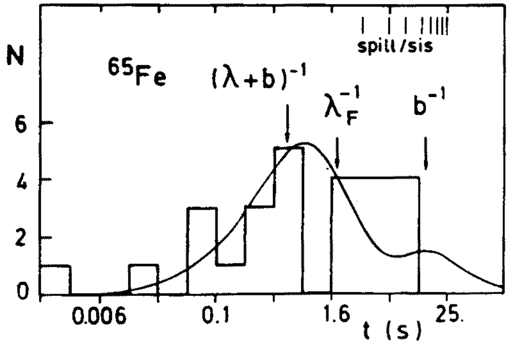

Fig. 11. Time distribution for the ^{65}Fe decays plotted in logarithmic bins. The background is marked with *b*.

Very recently, a detailed investigation of the β-delayed proton emitter ^{37}Ca, including γ-transitions and branching ratios, was carried out. The understanding of the β matrix elements is the key to the understanding of the neutrino capture of ^{37}Cl, used as neutrino detector [37]. The on-line measurement of the half-life gives a value shorter than the literature value, which implies a lower sensitivity of the ^{37}Cl neutrino detector than accepted today. Nuclear masses can be directly measured for nuclei circulating in the storage ring ESR. The mass M and the velocity v of an ion coasting in the ring are related by:

$$\frac{\Delta M}{M} = \gamma_{\rm tr}^2 \left[\left(\frac{\Delta T}{T}\right)^2 + \left(1 - \frac{\gamma^2}{\gamma_{\rm tr}^2}\right) \left(\frac{\Delta v}{v}\right)^2 + \left(\frac{\Delta B}{B}\right)^2 \right]^{1/2} , \qquad (5)$$

where T is the time resolution of the setup, $\gamma_{\rm tr}$ is the transition γ of the ring, *i.e.* the mode for isochronous circulation of the ions, and B is the magnetic field.

Two different methods for direct mass measurement of ions stored in the ESR have been proposed: either to operate the ring at the transition energy and to measure the revolution frequency of single ions with thin time-of-flight detectors event by event [39] or to minimize the velocity spread by the application of beam cooling [40].

A pilot experiment to investigate the possibility to store and cool secondary-beams was performed successfully. A ^{20}Ne beam and its fragments with the same A/Z ratio, A/Z=2, were stored and cooled simultaneously [42]. Fig. 12 shows a Schottky spectrum of the circulating beam where shift of the mass lines due to the different binding energy is nicely seen. In later experiments it was demonstrated that the momentum spread of a cooled beam is of the order of 10^{-6} [40]. With such a resolution the desired precision of 200 keV can be obtained for masses up to 200. The resolution of the time-of-flight method is expected to be lower by one order of magnitude. The advantage is the applicability to short half-lives down to several microseconds, determined by the time needed for some ten turns in the ring.

The time for the cooling of stored ions in a storage ring by interaction with an electron current of the density j is

$$t_0 = 3 \cdot 10^7 \beta^4 \gamma^8 \frac{A}{j \eta Z^2} \left(\frac{\Delta p}{p}\right)^3 \frac{s}{{\rm cm}^2 A} , \qquad (6)$$

where A and Z are mass and charge, β is the particle velocity normalized to the velocity of light, $\gamma = \frac{1}{\sqrt{1-\beta^2}}$ and η is the length of the cooler section in units of the ring circumference. Note that the cooling time decreases with Z^2 but increases with the third power of the momentum spread of the ions to be cooled. The cooling time for a bismuth beam was a few hundred milliseconds [40].

6.2. Interaction of the nucleus with its electron cloud

An exciting experiment carried out in the storage ring was the discovery of the beta-decay into bound electron states [41]. The weakly bound

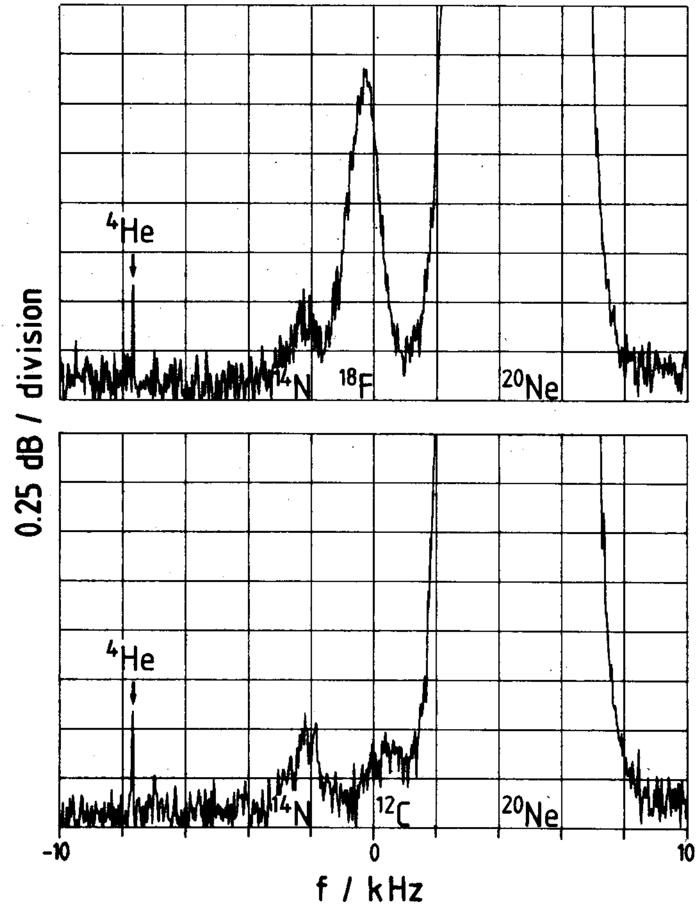

Fig. 12. Schottky spectrum of ^{20}Ne and its fragments with $A/Z = 2$ stored and cooled in the ESR. Upper panel: after cooling, lower panel: after 12 h storage.

isotope ^{163}Dy becomes instable when it is fully stripped: Because of the low Q-value, the small energy of the β-decay is not sufficient to reach the continuum: This stabilizes the dysprosium as a neutral atom against its decay. When, however, the inner orbitals are free and accessible to the decay electron it can escape and the nucleus becomes unstable.

The opposite effect will be observed for exotic nuclei decaying by electron capture. Being bare they will become stable. Their half-lives can be varied by changing the electron density in the vicinity of the nucleus, *e.g.* by attaching one, two or more electrons. The investigation of such highly stripped β-decaying nuclei will not only yield new data, as small branching ratios, but hopefully lead to a better understanding of β-decay.

6.3. Direct reactions

Nuclear reaction studies in inverse kinematics with cooled beams circulating in the ESR and using the internal gas-target are in preparation. We will investigate the nuclear structure in direct reactions such as inelastic proton scattering (p,p') and nuclear transfer (d,p) [43]. With electron cooling, highly brilliant beams with opening angles of less than 0.05 mrad and spotsizes below 1 mm have been obtained inside the ESR [40]. Experiments with the internal gas target with densities of $10^{13}/\mathrm{cm}^2$ to $10^{14}/\mathrm{cm}^2$ yield effective target thicknesses of $10^{19}/\mathrm{cm}^2$ to $10^{20}/\mathrm{cm}^2$ for the ions circulating with 10^6 revolutions per second. This technique permits extremely high resolution experiments not suffering from atomic scattering, as permanent beamcooling restores the beam after its passage through the target.

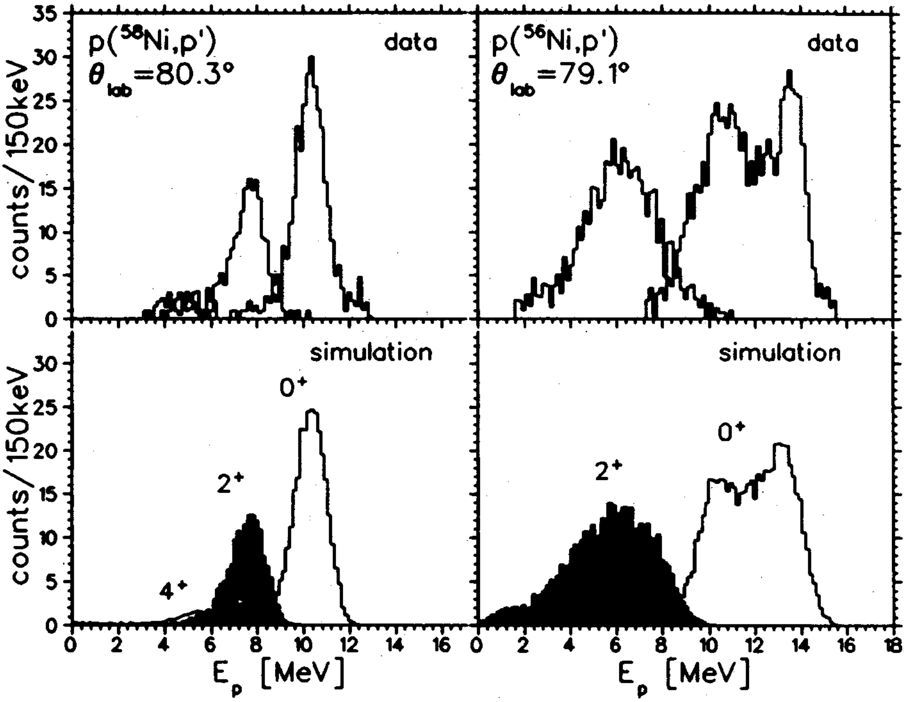

Fig. 13. Energy spectra for the left hand side: $p(^{58}\mathrm{Ni},p')^{58}\mathrm{Ni}$ at $\Theta_{\mathrm{lab}} = 80.3$ and 101 MeV/u, and the right hand side: $p(^{56}\mathrm{Ni},p')^{56}\mathrm{Ni}$ at $\Theta_{\mathrm{lab}} = 79.1$ and 101 MeV/u. Upper part: experiment, lower part: Monte Carlo simulation [44].

A first pilot (p,p') experiment on the doubly magic instable nucleus ^{56}Ni has been carried out directly behind the fragment separator. The proton spectra for the scattering on the stable ^{58}Ni and the unstable ^{56}Ni are displayed in Fig. 13 [44]. From these data the B(E2) value of 850±120 e^2fm^2 was extracted, which has to be compared with the limit of B(E2) $\geq$ 230 e^2fm^2.

A first experiment using the internal gas-target will be the inelastic proton scattering on ^{56}Ni to investigate transitions to unnatural parity states, like the 1^+ magnetic dipole state [45].

7. Experiments in the target hall — inclusive measurements and γ-spectroscopy

With secondary-beams directed to the target hall, *e.g.* to the 4π cave equipped with the combination of the ALADIN magnet and the LAND large area neutron detector, a continuation of our secondary-beam experiments is planned. The aim of these experiments is the investigation of neutron drip line nuclei beyond beryllium. Again, the transverse momenta and the neutron correlations measured with ALADIN and LAND will be companion experiments with the fragment separator where the longitudinal momentum spreads will be measured.

The completion of this setup by the Heidelberg Crystal Ball will extend our possibilities for in-beam gamma spectroscopic experiments with relativistic ions of exotic nuclei, a new field of nuclear spectroscopy. It concentrates on the investigation of collective states such as the first excited 2^+ states in even nuclei and giant resonances, the decay of which is expected to populate low spin states.

8. Conclusion

Already the first experiments at the projectile fragment separator gave interesting results and showed new perspectives of secondary-beam physics at relativistic energies. Isotopic projectile fragment beams throughout the whole periodic table up to uranium are available for the first time. The purity of these beams allows the measurements of nuclear ground state properties with high sensitivity.

New nuclear structure information will be obtained from reaction studies with instable nuclear beams as *e.g.* the measurement of interaction radii, breakup after peripheral interactions or Coulomb excitation, elastic and inelastic scattering in reversed kinematics and in-beam gamma spectroscopy.

Putting together all this information to a consistent picture will help us to understand nuclear properties and to improve nuclear models.

I acknowledge fruitful discussions with P. Armbruster, H. Geissel, K. Sümmerer and K.H. Schmidt. I thank E. Pfeng for his assistance in preparing the manuscript.

REFERENCES

[1] H. Geissel *et al.*, *Nucl. Instr. Meth.* **B70**, 286 (1992).

[2] M. Pfützner *et al.*, Proc. 22nd Mazurian Lakes Summer School, Piaski, 1991, Institute of Physics Publishing, New York 1992, p.339.

[3] A. Magel *et al.*, GSI annual report 1993 GSI93-1,23.

[4] P. Armbruster *et al.*, GSI annual report 1992 GSI93-1,28 .

[5] S. Kox *et al.*, *Nucl. Phys.* **A420**, 162 (1984).

[6] M. Weber, thesis Technische Hochschule Darmstadt, Int. Report 1993, GSI-93-26.

[7] J. Friese *et al.*, GSI annual report 1992 GSI93-1,25.

[8] K.H. Schmidt *et al.*, *Phys. Lett.* **B300**, 313 (1993).

[9] G. Rudstam, *Z. Naturf.* **21a**, 1027 (1966).

[10] R. Silberberg, C.H. Tsao, *Asstrophys. J. Suppl.* **25**, 315, 355 (1973).

[11] K. Sümmerer *et al.*, *Phys. Rev.* **C42**, 2546 (1990).

[12] J. Friese *et al.*, Proc. XXXI Winter Meeting on Nuclear Physics, Bormio 1993, in press.

[13] J.D. Bowman *et al.*, Int. Rep. Lawrence Berkeley laboratory, 1958, LBL-2908.

[14] N. Metropolis *et al.*, *Phys. Rev.* **C110**, 185, 204 (1958).

[15] J.J. Gaimard *et al.*, *Nucl. Phys.* **A531**, 709 (1991).

[16] X. Campi *et al.*, *Phys. Rev.* **C24**, 2199 (1981); *Phys. Rev.* **B300**, 313 (1993).

[17] M. Fauerbach, Diplom Thesis Technische Hochschule Darmstadt 1992, unpublished.

[18] J. Huebele *et al.*, accepted for publication in *Phys. Rev.* C.

[19] Y. Yariv *et al.*, *Phys. Rev.* **C20**, 2227 (1979).

[20] A. Gavron, *Phys. Rev.* **C12**, 230 (1980).

[21] M. Weber *et al.*, GSI annual report 1992 GSI93- 1,30.

[22] D.J. Morrissey, *Phys. Rev.* **C39**, 460 (1989).

[23] A.S. Goldhaber *Phys. Lett.* **53B**, 306 (1974).

[24] I. Tanihata *et al.*, *Phys. Lett.* **B160**, 380 (1985):*Phys. Rev. Lett.* **55**, 2676 (1985).

[25] H. Sagawa, *Phys. Lett.* **B286**, 7 (1992).

[26] P.G. Hansen, *Nucl. Phys.* **A553**, 89 (1993).

[27] B. Blank *et al.*, *Z. Phys.* **A340**, 41 (1991).

[28] I. Tanihata, *Nucl. Phys.* **A553**, 361 (1993).

[29] I. Tanihata, private communication 1991.

[30] A. Chulkov, private communication 1991.

[31] R. Anne *et al.*, *Phys. Lett.* **250**, 19 (1990).

[32] N.A. Orr *et al.*, *Phys. Rev. Lett.* **69**, 2050 (1992).

[33] A. Seliverstov, S. Neumeier, private communication 1993.

[34] W. Schwab *et al.*, GSI annual report 1992 GSI93-1,22.

[35] F. Humbert *et al.*, GSI annual report 1992 GSI93-1,21.

[36] R. Anne *et al.*, *Phys. Lett.* **250**, 19 (1990).

[37] E. Adelberger, private communication 1993.

[38] S. Czajkovski *et al.*, Proc. Int. Symp. on Nuclear and Astrophysics, Karlsruhe, Germany 1992, Institute of Physics Publishing, New York 1993.
[39] J. Trötscher *et al.*, *Nucl. Instr. Meth.* **B70**, 455 (1992).
[40] B. Franzke, Proc. 3rd European Perticle Acelerator Conference, Berlin, Germany, 1993, GSI Preprint GSI-92-15.
[41] M. Jung *et al.*, *Phys. Rev. Lett.* **69**, 2164 (1992).
[42] H. Geissel *et al.*, *Phys. Rev. Lett.* **68**, 3412 (1992).
[43] P. Egelhof, Proc. Int. Worksh. on the Physics and Techniques of secondary Beams, Dourdan 1992, Editions Frontiers, Gif-sur Yvette, 1993, p.1780.
[44] G. Kraus *et al.*, GSI Annual Report 1992 GSI93-1.
[45] J. Friese, private communication 1993.